Nanoscale

PAPER

View Article Online
View Journal

Cite this: DOI: 10.1039/d5nr05371d

Wastewater to hydrogen: iron–nickel electrocatalysts fabricated by a green synthesis achieving industrial current densities

Thomas Karagiannis,[a] Eamonn Devlin,[b] Aran Rafferty,[c] Raman Bekarevich,[d] Vassilis Psycharis,[b] Vasileios Tzitzios,[a,b] Aphrodite Tomou,[e] Rocco Villano,[f] Leila Negahdar[f] and M. Veronica Sofianos *[a]

The development of sustainable hydrogen production technologies is crucial to address the global energy crisis and reduce carbon emissions. With growing concerns over freshwater scarcity, the combination of green hydrogen production with ammonia oxidation reaction from wastewater, emerges as a highly promising strategy for meeting carbon goals and reusing treated water. Here, we report a green, scalable, room-temperature chemical reduction method for the successful synthesis of self-supported FeNiB, FeNiBP, and FeNiP electrocatalysts on nickel foams. FeNiB@NF exhibited the highest HER activity, achieving −469 mA cm^{-2} at −0.71 V *vs*. RHE with an overpotential of −0.26 V *vs*. RHE at −100 mA cm^{-2} in alkaline water and −330 mA cm^{-2} at −0.69 V *vs*. RHE and with an overpotential of −0.34 V *vs*. RHE at −100 mA cm^{-2} in ammonia-rich electrolyte, while FeNiBP@NF delivered superior OER performance of 972 mA cm^{-2} at 2.3 V *vs*. RHE and AOR performance of 963 mA cm^{-2} at 1.97 V *vs*. RHE. Physicochemical analysis further revealed that the strong reducing power of sodium borohydride was crucial in generating metallic Fe and Ni states, underpinning the outstanding activity of FeNiB@NF in HER. On the other hand, the synergistic effects of boron and phosphorus in FeNiBP@NF likely facilitated OH* and NH_3* adsorption, contributing towards its high catalytic activity in OER and AOR, respectively.

Received 19th December 2025,
Accepted 13th April 2026

DOI: 10.1039/d5nr05371d

rsc.li/nanoscale

Introduction

The unstoppable growth of energy demand, together with the urgent necessity to reduce carbon emissions, has accelerated the rapid need to transition towards a sustainable energy future. Among the various proposed clean energy alternatives, green hydrogen (H_2) is considered a key player for a future carbon-neutral economy, due to both its high gravimetric energy density (120 MJ kg^{-1}), and its usage of zero greenhouse gas emissions.[1,2] Specifically, green hydrogen is produced from electrochemical water splitting using renewable energy sources. At the cathode, hydrogen is produced through the hydrogen evolution reaction (HER), and at the anode, oxygen is generated through the oxygen evolution reaction (OER), with an overall thermodynamic cell potential of 1.23 V *vs*. RHE. However, the commercial viability of green hydrogen is significantly hindered by the OER's sluggish four-electron transfer kinetics, requiring in reality additional energy to run the process, which results in an overall cell potential higher than 1.6 V *vs*. RHE.[3] Furthermore, it is crucial to take under serious consideration the immense global water scarcity. As a result, the reliance on purified water as a feedstock for large-scale green hydrogen production presents a significant sustainability challenge.[4,5] Consequently, coupling the HER with a thermodynamically more favourable anodic reaction that does not require ultra-pure water as feedstock, can be an attractive alternative.

The ammonia oxidation reaction (AOR), particularly utilising ammonia-rich industrial or municipal wastewater, has emerged as a notable substitute for the OER. This integrated approach offers a threefold advantage. First, it enables hydrogen production at a significantly lower cell voltage. In detail, the theoretical thermodynamic potential of AOR is 0.06 V *vs*. RHE, which is much lower compared to the 1.23 V *vs*. RHE for OER. Second, toxic ammonia-rich wastewater streams can be utilised, facilitating their remediation.[6,7] Third, ammonia elec-

[a]*School of Chemical and Bioprocess Engineering, University College Dublin, Belfield, Dublin 4, Ireland. E-mail: veronica.sofianos@ucd.ie*
[b]*Institute of Nanoscience and Nanotechnology, N.C.S.R. Demokritos, 15341 Agia Paraskevi, Athens, Greece*
[c]*AMBER Research Centre, Naughton Institute, Trinity College Dublin, Dublin 2, D02PN40, Ireland*
[d]*Advanced Microscopy Laboratory, Centre for Research on Adaptive Nanostructures and Nanodevices (CRANN), Trinity College Dublin, Dublin 2, Ireland*
[e]*Goodfellow, Ermine Business Park, Huntingdon, Cambs, PE29 6WR England, UK*
[f]*School of Chemistry, University College Dublin, Belfield, Dublin 4, Ireland*

trolysis inherently enhances safety by preventing the formation of an explosive H_2/O_2 mixture.[8] Despite these benefits, AOR suffers from sluggish kinetics, a complex multistep reaction pathway, and challenges related to catalyst selectivity, poisoning, and bifunctionality for simultaneous ammonia oxidation and hydrogen evolution.[9,10] To overcome these barriers, considerable effort has been dedicated to the rational design of advanced electrocatalysts. An ideal electrocatalyst must be cost-effective and exhibit high intrinsic activity, excellent selectivity towards N_2 to avoid the formation of NO_x intermediates, and long-term stability under harsh operating conditions, as illustrated in Fig. 1.[8,11,12] The benchmark electrocatalysts for AOR to date are platinum-group metals (PGMs), such as Pt and its alloys, which demonstrate excellent activity. Nonetheless, the industrial application of these noble metals electrocatalysts is severely restricted by their scarcity, high cost, and poor long-term stability.[5,13,14] Hence, the development of earth-abundant alternatives is imperative in order to materialise large-scale green hydrogen production through wastewater electrolysis. Transition metal (TM)-based compounds, including borides, phosphides, nitrides, sulphides, hydroxides, and carbides, have been identified as a highly promising class of materials that can deliver enhanced catalytic activity at a fraction of the cost of PGMs.[15–18] Specifically, transition metal borides (TMBs) and phosphides (TMPs) have gained significant attention for their exceptional performance in HER and OER, attributed to their unique electronic structures, high intrinsic activity, and excellent stability in alkaline conditions.[18,19] The incorporation of boron into TMBs can modulate the electronic structure of metal centres, optimise the adsorption of reaction intermediates, and improve their electrical conductivity and overall stability.[20] Similarly, the promotional effect of phosphorus in TMPs is often attributed to its moderate electronegativity, which can optimise the electronic structure of the transition metal centre, providing both proton-acceptor and hydride-acceptor centres to facilitate the HER.[21] For anodic reactions such as OER and AOR, it is widely accepted that TMBs and TMPs undergo *in situ* surface reconstruction during the electrochemical process, forming a thin layer of amorphous metal-(oxy)hydroxides, which are considered the true catalytically active species.[22,23]

On the other hand, the development of bimetallic systems has proven to be a particularly effective strategy to enhance the electrocatalytic activity of single-metal catalysts, as the synergistic coupling between two distinct metals results in an electrocatalytic performance far exceeding that of their monometallic counterparts.[11,24] This enhancement can be attributed to improved conductivity, greater stability and the presence of dual active sites. For example, K. Jiang *et al.* demonstrated that $NiCo_2N$ on nickel foam (NF) achieved a current density of 100 mA cm^{-2} at 1.74 V *vs.* RHE and 0.71 V *vs.* RHE at an H-shape cell for water and ammonia electrolysis respectively.[25] C. Jo *et al.* integrated N and C active sites in Ni_2P and reached a current density of 10 mA cm^{-2} at 400 mV for OER *vs.* RHE and 210 mV for AOR *vs.* RHE. For HER the overpotential required at 10 mA cm^{-2} was 161 mV *vs.* RHE.[26] A pioneering work from A. Ashok Kashale *et al.* synthesised a bifunctional NiCuBO/NF electrocatalyst for testing a two-electrode system, demonstrating a cell potential at 10 mA cm^{-2} for overall ammonia splitting equal to 1.56 V *vs.* RHE and 1.67 V *vs.* RHE for overall water splitting.[23] J. Wang *et al.* showed remarkable bifunctional activity for AOR and HER of B-NiFe-LDH/NF reaching 100 mA cm^{-2} at 1.381 V *vs.* RHE and an overpotential of 97 mV *vs.* RHE at 10 mA cm^{-2} respectively.[8] Such findings underscore the immense potential of multicomponent TM-based catalysts for challenging electrochemical reactions. Building on these foundations, the hypothesis was formed that a synergistic effect between boron and phosphorus within a bimetallic FeNi framework could unlock unprecedented catalytic activity for ammonia-assisted hydrogen production. The use of NF as a conductive substrate provides a robust, binder-free three-dimensional electrode with high surface area, facilitating mass transport and electron transfer.[27] Central to our approach is the development of a scalable, simple, and green synthesis methodology. We have adapted our previously reported one-step chemical reduction method, enabling the simultaneous incorporation of boron into the FeNi alloy at low temperatures.[28]

In this study, we demonstrate the successful synthesis of self-supported FeNi electrocatalysts on NF by modulating the B to P stoichiometric ratio *via* a scalable, room-temperature chemical reduction method. The influence of this B to P ratio on the electrocatalytic performance in alkaline media, both with and without ammonia, was investigate through electrochemical measurements and correlated with physiochemical characterisation to establish the structure/performance relationships. The electrocatalyst with a B/P = 1 stoichiometric ratio during synthesis, FeNiBP@NF, demonstrated the highest OER and AOR electrocatalytic performance achieving indus-

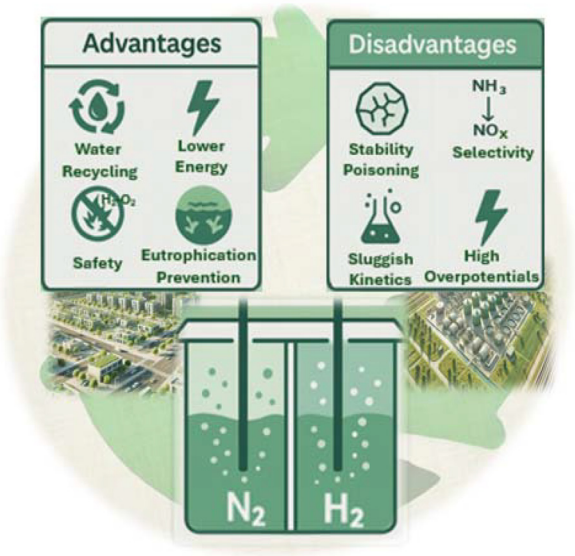

Fig. 1 Graphical representation of advantages and disadvantages of ammonia-rich electrolyser.

trial scale current densities of 972 mA cm^{-2} at 2.3 V *vs.* RHE and 963 mA cm^{-2} at 1.97 V *vs.* RHE, respectively. For alkaline water HER, the electrocatalyst with no amount of P, FeNiB@NF, exhibited a maximum current density of −469 mA cm^{-2} at −0.71 V *vs.* RHE and an overpotential of −0.26 V at −100 mA cm^{-2}. In ammonia-rich electrolyte, FeNiB@NF exhibited a current density of −330 mA cm^{-2} at −0.69 V *vs.* RHE and an overpotential of −0.34 V at −100 mA cm^{-2}. Hence, this study offers key insights into how the relative molar ratio of B to P in FeNi-based electrocatalysts can be precisely tuned to optimise performance for efficient water splitting in alkaline electrolytes, as well as hydrogen generation from ammonia-rich wastewater.

Experimental

Synthesis of self-supported bimetallic electrocatalysts

Initially, NF with dimensions of 1.5 cm × 0.5 cm (99.5% purity, ~0.9 mm thickness, Goodfellow Cambridge Ltd) was ultrasonically cleaned in acetone (C_3H_6O, 99.5% Lennox Laboratory Supplies Ltd) and then rinsed twice in deionised (DI) water for 5 minutes each time. Subsequently, it was ultrasonicated in a commercial 5% acidity spirit vinegar for 1.5 hours. The NF was then ultrasonically rinsed twice with DI water and absolute ethanol (C_2H_6O, 99.5% Sigma-Aldrich) for 5 minutes each time and dried at 85 °C under vacuum for 12 hours.

In line with green chemistry principles, both for the NF pretreatment and electrocatalysts synthesis, instead of using strong acids and solvents, we focused on low-impact acids and aqueous solutions. Additionally, all synthesis steps were performed at low temperatures to minimise energy consumption.[29]

The self-supported electrocatalysts were synthesised using a scalable one-pot chemical reduction method, as illustrated in Fig. 2. Initially, a sufficient quantity of DI water for the preparation of both the metal precursor solution and the reducing agent solution was degassed by nitrogen bubbling for 1.5 hours at 60 °C to ensure satisfactory oxygen removal. Afterwards, the NF pieces were submerged in a 250 mL two-neck round-bottom flask containing 20 mL of the degassed DI water brought to room temperature. Then, 5 mmol of iron chloride tetrahydrate ($FeCl_2{\cdot}4H_2O$, Sigma-Aldrich, 99%) and 4.5 mmol of nickel chloride hexahydrate ($NiCl_2{\cdot}6H_2O$, Sigma-Aldrich, 99%) were simultaneously added under continuous nitrogen bubbling and vigorous stirring to form the metal precursor solution, with an optimal Fe/Ni atomic ratio of 1/0.9, as reported by our team.[28]

For the FeNiB@NF self-supported electrocatalyst, an aqueous solution of 0.1 M sodium hydroxide (NaOH, Sigma-Aldrich, ≥98%) was prepared in a 250 mL two-neck round-bottom flask containing 60 mL of DI water to prevent hydrolysis of the reducing agent. Then, 60 mmol sodium borohydride ($NaBH_4$, Sigma-Aldrich, ≥98%) was added. This reducing agent solution was introduced dropwise into the metal precursor solution, as illustrated in Fig. 2. The immediate formation of hydrogen gas bubbles indicated the initiation of the reaction. After stirring for 2 hours under nitrogen bubbling, the FeNiB@NF electrodes were collected, washed twice with DI water and subjected to the same deposition process once more to achieve the desired electrocatalyst loading on the NFs. The double-loaded electrodes were washed again twice with DI water, once with pure ethanol and finally dried at 85 °C under vacuum in the electrocatalyst slurry for 12 hours. Similarly, the remaining electrocatalyst slurry was washed using the aforementioned method and collected *via* centrifugation at 6000 rpm for 5 minutes.

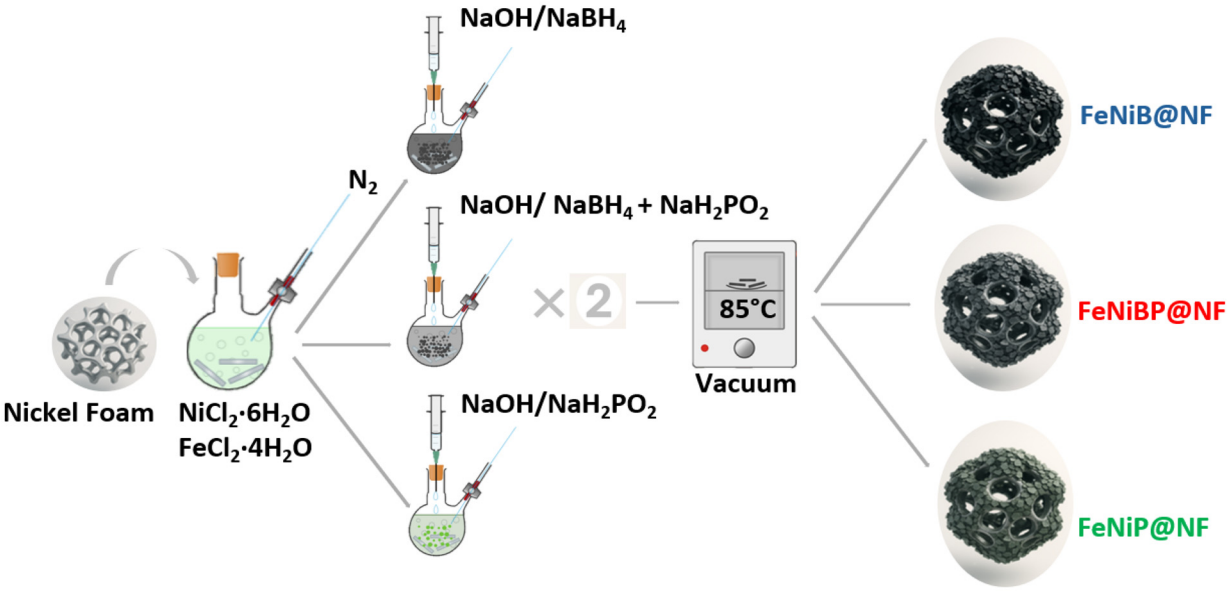

Fig. 2 Synthesis procedure of self-supported bimetallic electrocatalysts.

For the synthesis of FeNiP@NF, the same methodology was followed, replacing sodium borohydride with 60 mmol sodium hypophosphite (NaH_2PO_2, Sigma-Aldrich, anhydrous, 98–101%). Finally, the FeNiBP@NF was synthesised by adjusting the boron-to-phosphorus molar ratio to 1/1 while maintaining the concentration of the reducing agents at 1 M and keeping the solution temperature at 50 °C throughout the double synthesis procedure. The molar ratios of reducing agents and the nomenclature of the electrocatalyst are indicated in Table 1.

Materials characterisation

X-ray powder diffraction (XRD) measurements were performed on a SmartLab θ/θ Bragg–Brentano Rigaku diffractometer equipped with a pyrolytic graphite monochromator positioned on the diffracted beam path, employing Cu Kα radiation (Cu-$K_\alpha1$ = 1.54060 Å, Cu-$K_\alpha2$ = 1.54439 Å). Prior to analysis, all samples were homogenised by gentle grinding in an agate mortar, and the resulting fine powders were mounted onto standard aluminium sample holders. The diffractometer was operated at an accelerating voltage of 40 kV and a tube current of 35 mA, with divergence, scattering, and receiving slits set to 2/3°, 2/3°, and 0.6°, respectively. Data acquisition was carried out in a continuous step-scan mode with a step size of 0.03° and a counting time of 5 s per step, over a 2θ angular range of 20–80°.

Morphological observations were carried out using a Zeiss Sigma 300 scanning electron microscope (SEM). To prepare the SEM samples, the as-prepared electrocatalysts were placed on carbon tape and coated with a 4 nm platinum layer to enhance conductivity and minimise charging effects during imaging. Transmission Electron Microscopy (TEM) was utilised to analyse the morphology using a FEI Tecnai 20 microscope. Elemental mapping conducted using a FEI Titan 80–300 kV FEG S/TEM, integrated with an 'Element' EDX detector. Samples were first dispersed in isopropanol, ultrasonicated for 30 minutes, then deposited onto a 200-mesh carbon-coated copper grid (Mason Technology) and dried overnight at ambient conditions. For the determination of the specific surface areas and pore structures, nitrogen adsorption/desorption measurements at 77 K were conducted on a Nova 2400e analyser (Quantachrome, UK). The Brunauer–Emmett–Teller (BET)[30] method was applied to adsorption data in the 0.10–0.30 relative pressure range, while Barrett–Joyner–Halenda (BJH)[31] analysis of desorption isotherms provided pore size distributions and volumes in micro- and mesoporous ranges. Samples underwent degassing at 150 °C under vacuum for 4 hours prior to analysis. For the investigation of macroporosity, mercury porosimetry (Autoscan-33, Quantachrome) was used due to its much larger pore diameter measurement range, *i.e.* 7 nm–8000 nm approx. The pore diameter is based on the Washburn equation:

$$\text{Pore diameter}, D = (-4\gamma \cos\theta)/P \quad (1)$$

where θ is the contact angle (140°) between the sample and mercury, γ is the surface tension of mercury, taken as 485 dyn cm^{-1} and P (ranging between 0 and 33 000 psi) is the applied pressure needed for mercury to intrude into pores and interparticle voids.

X-ray photoelectron spectroscopy (XPS) was performed on a Kratos AXIS Ultra DLD spectrometer equipped with an Al Kα source (1486.7 eV) under ultra-high vacuum conditions to characterise the chemical composition of both electrocatalyst powders prior to electrolysis and self-supported electrodes after chronoamperometry testing. Data analysis was carried out using CasaXPS software, with all spectra calibrated to the adventitious C 1s peak at 284.5 eV. Mössbauer spectra were collected to further study the electronic state of iron in the FeNi electrocatalysts using a conventional transmission spectrometer with a ^{57}Co(Rh) source moving with constant acceleration at RT and 125 K. Isomer shifts are given with respect to metallic iron at RT. Mössbauer spectra were least-squares fitted using the IMSG program.[32]

Table 1 B/P synthesis ratio specification of as made electrocatalysts

Reducing agent concentration	B/P molar ratio	Electrocatalyst
60 mmol $NaBH_4$	1/0	FeNiB@NF
30 mmol $NaBH_4$ + 30 mmol NaH_2PO_2	1/1	FeNiBP@NF
60 mmol NaH_2PO_2	0/1	FeNiP@NF

Electrochemical measurements

All electrochemical measurements were conducted three times to ensure reliability at room temperature using a typical three-electrode cell connected to an Autolab potentiostat system (PGSTAT204 equipped with FRA32M Module, Metrohm) operated by a PC with Nova 2.1.7 software installed. As the reference electrode, a leakless silver/silver chloride (Ag/AgCl, 3 M KCl, Metrohm) electrode was used, whereas a graphite rod (MW-4131, BASi) was served as the counter electrode. The experiments utilised two different electrolyte solutions: an alkaline solution of 1 M potassium hydroxide (KOH, Sigma Aldrich, 90%, pH 14), and an alkaline ammonia-rich solution consisting of 1 M KOH + 0.33 M NH_3 (ammonium hydroxide solution, BioUltra, ~1 M NH_3 in H_2O, Sigma Aldrich). As benchmark electrocatalysts for OER and HER, RuO_2 (99.9%, Sigma-Aldrich) and Pt/C (10 wt% Pt on carbon, Sigma-Aldrich) were used, respectively. For the RuO_2 and Pt/C electrode preparation, 5 mg of the aforementioned electrocatalysts powders was dispersed in 490 μL of DI water, 490 μL of absolute ethanol, and 20 μL of 5 wt% Nafion (Sigma-Aldrich). The suspensions were sonicated in an ultrasonic bath for 30 min to ensure uniform dispersion. Then, 10 μL of the ink was drop-cast onto a 5 mm glassy carbon (GC) rotating disk electrode from Metrohm, with a total geometric area of 0.2 cm^2 serving as the working electrode and dried under an IR lamp.

All potentials were standardised relative to the reversible hydrogen electrode (RHE) using the equation: $E_{RHE} = E_{(Ag/AgCl)} + 0.197 + 0.059 \times pH$. E_{RHE} denotes the potential *versus* RHE,

$E_{(Ag/AgCl)}$ represents the measured potential *versus* the Ag/AgCl (3 M KCl) reference electrode, 0.197 V is the standard potential of Ag/AgCl (3 M KCl) at 25 °C, and 0.059 V is the Nernst slope per pH unit.

Linear sweep voltammetry (LSV) was performed at a scan rate of 5 mV s^{-1} after degassing the electrolyte for 15 minutes under a nitrogen atmosphere (>99.999%, BOC) to assess HER, OER and AOR catalytic performance of the electrocatalysts. The reported Tafel slopes were calculated from a limited linear region of the LSV curves, as per common practice for comparative analysis of electrocatalysts. As such, these values are used primarily for relative comparison between the samples, rather than as absolute kinetic descriptors.

Electrochemical impedance spectroscopy (EIS) measurements were taken at 0 V, employing an AC amplitude of 10 mV over a frequency range from 100 kHz to 100 mHz. The uncompensated resistance (R_s) normalised by the geometrical area (0.5 cm^2) was obtained from normalised Nyquist plots and subsequently used to correct the ohmic drop in potential measurements with the formula: $E_c = E_e - (i \times R_{s,\ norm})$.[33] Where, E_c is the corrected potential and E_e the experimentally measured potential. The stability of the electrocatalysts was examined through 24 hour chronoamperometry tests. Additionally, cyclic voltammetry (CV) was employed to estimate the electrochemically active surface area (ECSA) of each electrocatalyst. CV measurements were conducted at scan rates of 20, 40, 60, 80, 100, and 120 mV s^{-1} within the non-Faradaic current region (0.87–1.17 V *vs.* RHE). From these scans, the difference between anodic and cathodic current densities (Δj) at 1.02 V *vs.* RHE was plotted against scan rate, and the slope obtained was multiplied by the geometric electrode surface area to calculate the double-layer capacitance (C_{dl}). The ECSA was determined by the equation ECSA (cm^2) = C_{dl}/C_s, where C_s is the standard specific capacitance with a value of 40 μF cm^{-2} for a flat surface at pH 14.

Operando diffuse reflectance Fourier transform infrared spectroscopy (DRIFTS) was performed using a Bruker Vertex 70 spectrometer equipped with a liquid-nitrogen-cooled HgCdTe (MCT) detector and connected to a customised flow cell assembly. The electrode was mounted in the DRIFTS chamber with its upper surface exposed to the infrared beam. During the measurement, LSV from 0 to 2 V (*vs.* Ag/AgCl) and a scan rate of 5 mV s^{-1} in both 1 M KOH and 1 M KOH + 0.33 M NH_3 electrolytes was conducted. The counter electrode was positioned in an isolated compartment to prevent cross interaction with the working electrode. Each spectrum was recorded by averaging 64 scans at a spectral resolution of 4 cm^{-1} over the 4000–400 cm^{-1} range. Spectra were acquired at 15 second intervals throughout the LSV, and each dataset was matched to the corresponding applied potential to generate a potential-resolved vibrational map, allowing the observation of key reaction intermediates involved in OER and AOR.

Cell potential polarisation measurements were performed in a two-electrode configuration with a distance of 25 mm between the electodes. The applied potential ranged from 0 to 2.0 V at a scan rate of 5 mV s^{-1}, without applying any *iR* correction.

Results and discussion

The bimetallic-based electrocatalysts (FeNiB, FeNiBP, and FeNiP) were synthesised and directly embedded onto NFs by performing a simple green synthesis method. The proposed reduction mechanisms (reactions 2, 3 and 4) lead to the formation of the bimetallic-based electrocatalysts (FeNiB, FeNiBP, and FeNiP) along with byproducts such as sodium chloride (NaCl), boric acid (H_3BO_3), phosphorous acid (H_3PO_3), and hydrogen gas (H_2). All NaCl, H_3BO_3 and H_3PO_3 are water soluble and can be removed by washing the collected nanoparticles, while the hydrogen gas escapes during the synthesis process.

$$FeCl_2 + NiCl_2 + 4NaBH_4 + 9H_2O \quad (2)$$

$$FeCl_2 + NiCl_2 + 2NaBH_4 + 2NaH_2PO_2 + 2H_2O \rightarrow FeNiBP + 4NaCl + 5H_2 + H_3BO_3 + H_3PO_3 \quad (3)$$

$$FeCl_2 + NiCl_2 + 4NaH_2PO_2 + H_2O \rightarrow FeNiP + 4NaCl + 0.5H_2 + 3H_3PO_3 \quad (4)$$

The average self-supported electrocatalyst loading on NF for FeNiB@NF, FeNiBP@NF and FeNiP@NF was 5.4 mg cm^{-2}, 3.7 mg cm^{-2} and 3.1 mg cm^{-2}, respectively, as shown in Table S1.

Physicochemical analysis

X-ray diffraction (XRD) was recorded for all three electrocatalyst powders to assess their crystallinity (Fig. 3a–c). FeNiB (Fig. 3a) showed no distinct Bragg peaks, but only a broad peak was observed centred at 45° and expanding from 40° to 50°, consistent with an amorphous FeNiB phase commonly reported for metal borides with similar peak positioning to the FeNi phase (COD 96-901-0018). This might be due to the FeNiB having a lattice symmetry similar to the *P*4/*mmm* (no. 123) space group.[34,35] FeNiP (Fig. 3c), exhibited two broad asymmetrical peaks, one at around 30°–40° and the other at around 60° which could be assigned to amorphous FeNiP with similar peak positions as Fe_2P (COD 96-901-2124) with a $Pna2_1$ space group. Whereas, FeNiBP (Fig. 3b) exhibited additional diffraction peaks that may be attributed to amorphous iron nickel phosphates with similar peak positions as $Fe_2BP_3O_{13}$ (COD 96-222-8055) with a *P*63/*m* space group. Nevertheless, because all samples exhibit predominantly amorphous character, these assignments should be considered indicative only of possible local structures, rather than definitive crystalline phase identification.

SEM micrographs (Fig. 3d–f) show that all electrocatalysts are embedded successfully over the NFs. FeNiB@NF (Fig. 3d) forms discontinuous, cauliflower-like nanoparticle clusters that heavily roughen the NF stems and maximise interfacial area. On the other hand, FeNiBP@NF (Fig. 3e) yields a finer, more homogeneous granular film that covers the NF with fewer macroscopic voids, indicating improved deposition uni-

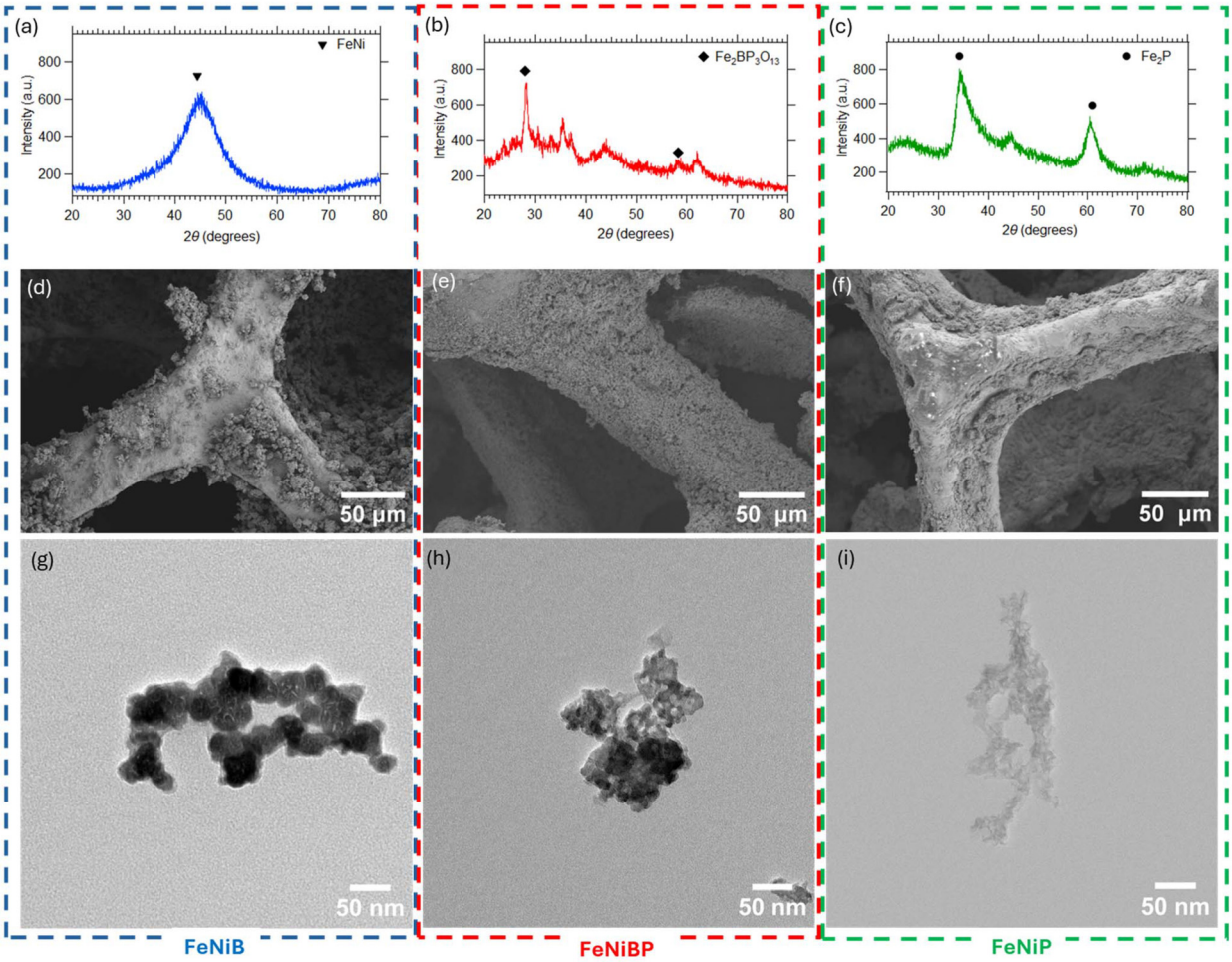

Fig. 3 XRD patterns of FeNiB (a), FeNiBP (b) and FeNiP (c). SEM images of FeNiB@NF (d), FeNiBP@NF (e) and FeNiP@NF (f). TEM images of FeNiB (g), FeNiBP (h) and FeNiP (i) self-supported bimetallic electrocatalysts.

formity. FeNiP@NF (Fig. 3f) appears denser and partially coalesced, with smoother regions punctuated by sporadic clusters, consistent with a more compact surface layer. To further evaluate this morphological distinctiveness of each self-supported electrocatalyst, N_2 adsorption–desorption measurements were performed to obtain BET surface area and BJH pore size distributions (Table 2). As shown in Table 2, FeNiP@NF exhibits the highest specific surface area of 23.4 $m^2\ g^{-1}$, followed by FeNiBP@NF with 14 $m^2\ g^{-1}$ and finally by FeNiB@NF with 11.8 $m^2\ g^{-1}$, indicating a decline in the specific surface area as the concentration of B in the B/P molar ratio increases from 0/1 to 1/0. The same trend is observed for the pore volume across the samples. The mode average pore diameter values, representing the highest data point on BJH graphs (Fig. S2a–c) are very similar between the electrocatalysts, confirming a mesoporous structure. These results support the TEM images which are described in detail in the following section and show that the FeNiP nanoparticles have a very fine 2D structure in comparison to the FeNiB and FeNiBP nanoparticles, hence it exhibits the highest specific surface area and pore volume. In addition, mercury porosimetry (Fig. S2d–f) revealed the presence of larger pores in FeNiB@NF with a mean pore diameter equal to 180 nm, reflecting the partial loading of the Ni foam, as shown in the corresponding SEM micrograph (Fig. 3d). The electrocatalysts with the second highest mean pore diameter (129 nm), according to mercury porosimetry, was FeNiP@NF. This value is also attributed to partial loading of the NF as shown in the respective SEM micrograph (Fig. 3f), similar to FeNiB@NF. Notably, FeNiBP@NF showed the smallest mean pore size of 92 nm, reflecting the homogenous distribution of FeNiBP particles on the Ni foam, as observed in Fig. 3e. It is important to note that the BET/BJH data obtained from N_2 adsorption–desorption measurements reflects the physical properties of the nanoparticles themselves, whereas the data obtained from mercury porosimetry is a measure of how well these nanoparticles are dispersed across the Ni foam, in terms of consistency and uniformity.

To assess the nanoscale morphology of the electrocatalysts, TEM images (Fig. 3g–i) were acquired. FeNiB (Fig. 3g) consists of aggregated spherical nanoparticles. Whereas, FeNiP (Fig. 3i)

Table 2 Self-supported electrocatalysts specific surface area, average pore size and pore volume

Electrocatalysts	BET specific surface area ($m^2\ g^{-1}$)	BJH pore volume ($cm^3\ g^{-1}$)	BJH pore size (mode) (nm)	BJH pore diameter (mean) (nm)	Porosimetry pore diameter (mean) (nm)
FeNiB@NF	11.8	0.042	3.7	13.9	180
FeNiBP@NF	14.0	0.045	3.7	12.3	92
FeNiP@NF	23.4	0.067	4.7s	11.3	129

is less heavily aggregated, with a flakier morphology. FeNiBP (Fig. 3h) appears intermediate between FeNiB and FeNiP, in terms of both aggregation and image contrast.

To better understand the morphological and structural characteristics of the FeNiBP sample, high-resolution TEM imaging and EDX elemental mapping were obtained. The HRTEM micrograph (Fig. 4b) appear to have no lattice fringes, thus validating the absence of crystal structure as shown in its associated XRD pattern (Fig. 3b). This is confirmed by the corresponding SAED pattern (Fig. 4c) since no distinctive diffraction rings appear. Elemental mapping (Fig. 4d) shows evenly dispersed Ni, Fe, B and P across the selected area of the nanoparticles, indicating no subgroup formations.

The surface chemical composition of FeNiB, FeNiBP, and FeNiP electrocatalysts was investigated using X-ray photoelectron spectroscopy (XPS). In the Fe 2p high-resolution spectra of Fe $2p_{1/2}$ and Fe $2p_{3/2}$ (Fig. 5a–c), the peaks around ~719.1 eV and ~706.2 eV are associated with metallic Fe for FeNiB (Fig. 5a), while the peaks at ~723.7 eV and ~710.6 eV are attributed to Fe^{2+} and the peaks at ~725.5 eV and ~712.4 eV correspond to Fe^{3+}, respectively. Two satellite peaks are observed at ~730.0 eV and ~715.0 eV. For FeNiBP (Fig. 5b), the Fe 2p spectrum of Fe $2p_{1/2}$ and Fe $2p_{3/2}$ shows two satellite peaks at ~730.9 eV and ~717.8 eV, along with Fe^{2+} at ~725.1 eV and ~712.0 eV, Fe^{3+} at ~725.3 eV and ~712.2 eV, respectively. In FeNiP (Fig. 5c), the Fe 2p spectrum of Fe $2p_{1/2}$ and Fe $2p_{3/2}$ shows two satellite peaks at ~736.5 eV and ~720.0 eV for Fe, with Fe^{3+} appearing at ~726.9 eV and ~713.6 eV, respectively.[28,36–38] No metallic Fe is present in FeNiBP and FeNiP electrocatalysts. This trend can also be observed in the Ni 2p spectra. The Ni 2p spectra of Ni $2p_{1/2}$ and Ni $2p_{3/2}$ (Fig. 5d–f) display for FeNiB (Fig. 5d) two metallic peaks at ~869.9 eV and ~852.8 eV, two satellite peaks at ~878.6 eV and ~860 eV, and two Ni^{2+} peaks at ~873.4 eV and ~855.7 eV, respectively. For FeNiBP (Fig. 5e), the Ni 2p spectrum of Ni $2p_{1/2}$ and Ni $2p_{3/2}$ shows two satellite peaks at ~879.9 eV and

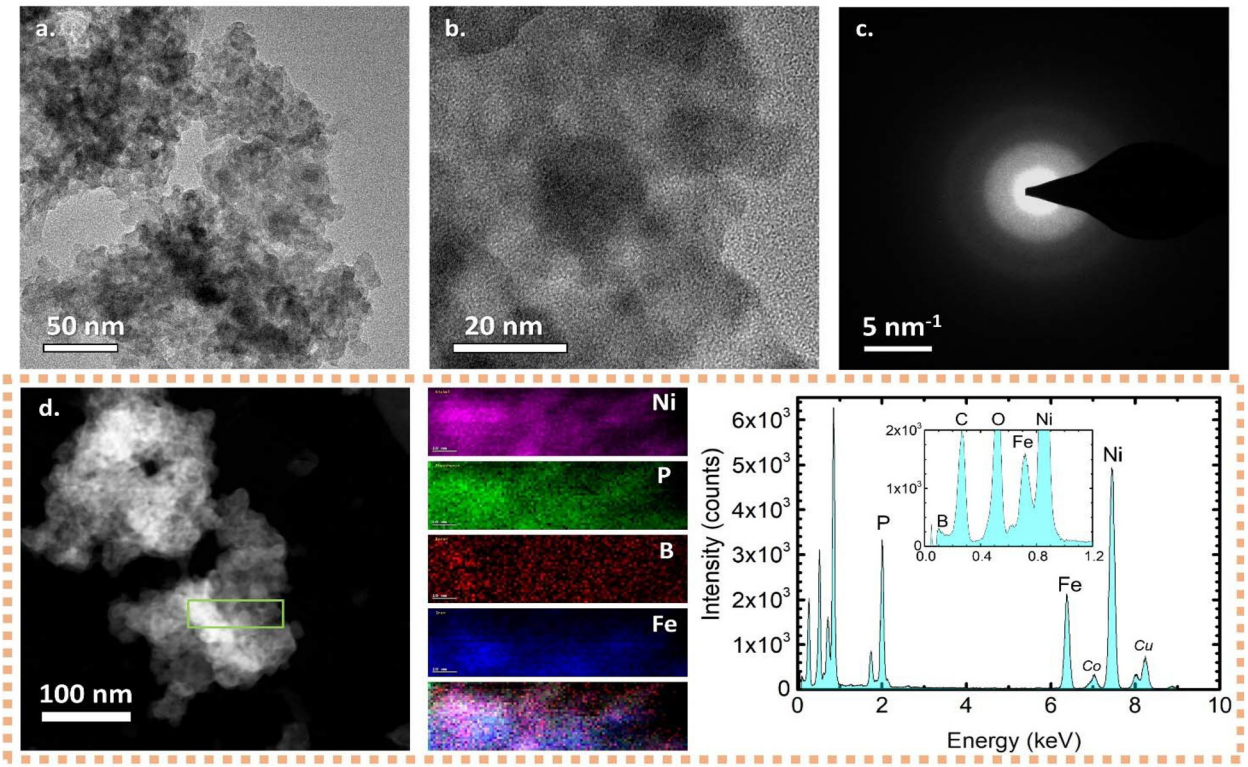

Fig. 4 The TEM micrograph (a), HTEM micrograph (b), SAED pattern (c), high angle annular dark field (HAADF), energy dispersive X-ray spectroscopy (EDAX-EDX) elemental mapping (d) for Ni, P, B, and Fe with an overlay (Ni/Fe/B/P).

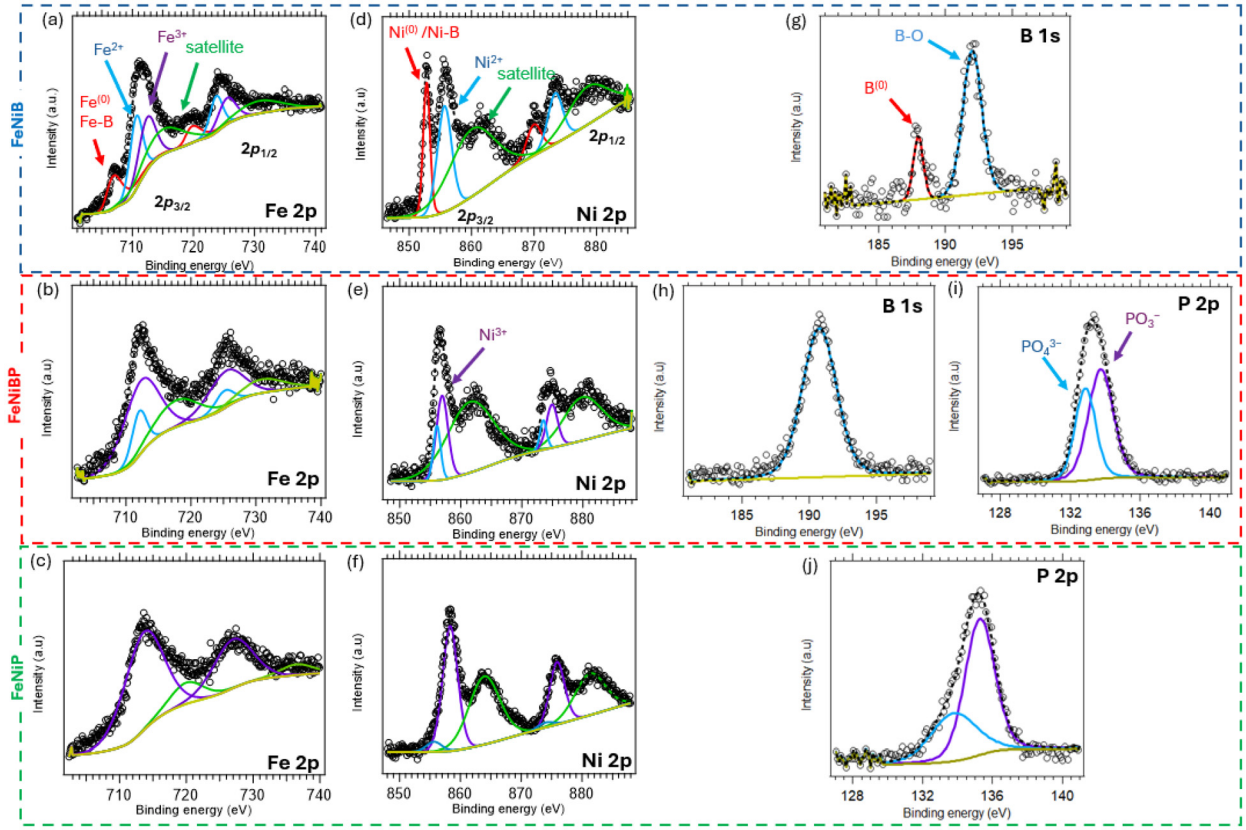

Fig. 5 High resolution XPS spectra of catalysts powders. Fe 2p of FeNiB (a), FeNiBP (b) and FeNiP (c), Ni 2p of FeNiB (d), FeNiBP (e) and FeNiP (f), B 1s of FeNiB (g) and FeNiBP (h), P 2p of FeNiBP (i) and FeNiP (j).

~861.5 eV, along with Ni^{2+} at ~873.5 eV and ~856.1 eV, and Ni^{3+} at ~874.9 eV and ~856.9 eV, respectively. In the Ni 2p of Ni $2p_{1/2}$ and Ni $2p_{3/2}$ spectra for FeNiP (Fig. 5f), the satellite peaks appear at ~881.3 eV and ~863.9 eV, with Ni^{2+} at ~874.0 eV and ~855.5 eV, and Ni^{3+} at ~875.9 eV and ~858.3 eV, respectively.[36,39] These results indicate that $NaBH_4$ is a stronger chemical reducing agent in comparison with sodium hypophosphite, and hence metallic Fe and Ni are formed in the FeNiB electrocatalyst, whereas in the FeNiBP and FeNiP electrocatalysts only Fe and Ni oxides are formed. Indicating that $NaBH_4$ is a stronger chemical reducing agent in comparison to NaH_2PO_2, and hence metallic Fe and Ni is formed in the FeNiB electrocatalysts, whereas in the FeNiBP and FeNiP electrocatalysts only Fe and Ni oxides were formed. This provides valuable information for the rational design of such electrocatalysts, as their surface chemistry can be easily tuned by selecting the appropriate chemical reducing agent during synthesis. Regarding the B 1s spectra for FeNiB (Fig. 5g), the peak at ~192.0 eV is assigned to the oxidised boron phase, while the peak at ~187.9 eV corresponds to metallic boron species, which is only present in FeNiB and in accordance with the Fe 2p and Ni 2p spectra. For FeNiBP (Fig. 5h), the B 1s spectrum shows no metallic boron, with a peak at ~190.7 eV corresponding to oxidised boron.[40] The P 2p spectra of FeNiBP (Fig. 5i) show peaks at ~133.7 eV for meta-phosphate (PO_3^-) and at ~132.9 eV for phosphate (PO_4^{3-}), while for FeNiP (Fig. 5j) peaks appear at ~135.2 eV for meta-phosphate (PO_3^-) and ~133.2 eV for phosphate (PO_4^{3-}), respectively.[36,41]

The valence states area percentages of Fe derived from XPS and Mössbauer spectroscopies including Ni area percentages derived from XPS for all three electrocatalyst powders, excluding oxygen contribution, are presented in Table 3. In detail, ^{57}Fe Mössbauer spectra were used to identify the Fe states in FeNiB, FeNiBP, and FeNiP (Fig. S3) through their isomer shift (IS) values. These data complement the XPS results regarding the nature of the iron species present in the FeNi electrocatalysts. According to the ^{57}Fe Mössbauer measurements, FeNiB contains both magnetic and paramagnetic contributions at room temperature (Fig. S3a) and at 125 K (Fig. S3b). In detail, two central doublets assigned to Fe^{3+} (~22% at RT, IS at RT = 0.35 mm s^{-1} and ~20% at 125 K), and Fe^{2+} (~5% at both RT and 125K, IS at RT = 0.92 mm s^{-1}), together with two broad, overlapping magnetic components (weighted average IS at RT = 0.11 mm s^{-1}) account for the remaining ~73–75% of the area. The almost unchanged component areas upon cooling argue against superparamagnetic relaxation. The near-metallic IS and broadened magnetic components (*i.e.* hyperfine field distribution) may arise from chemical disorder and non-stoichiometric Fe sites in an amorphous FeNiB phase. In contrast, FeNiP (Fig. S3d) is fully paramagnetic at room temperature,

Table 3 Electrocatalysts Fe and Ni valence states XPS spectra areas percentages and Fe site areas percentages derived from room temperature Mössbauer spectra

Electrocatalyst	Valence state	XPS 2p spectra area (%)	Mössbauer spectra area (%)
FeNiB	Fe (near-metallic)	25.3	73
	Fe^{2+}	37.8	5
	Fe^{3+}	36.9	22
	$Ni^{(0)}$	38.3	—
	Ni^{2+}	61.7	—
FeNiBP	Fe^{2+}	20.8	20
	Fe^{3+}	79.2	80
	Ni^{2+}	28.6	—
	Ni^{3+}	71.4	—
FeNiP	Fe^{3+}	100	100
	Ni^{2+}	6.9	—
	Ni^{3+}	93.1	—

described by two ferric doublets (spectral areas of ~54% and ~46%) that effectively form one broad Fe^{3+} distribution (weighted average IS at RT = 0.36 mm s^{-1}). FeNiBP (Fig. S3c) is also purely paramagnetic and fits to two doublets: Fe^{3+} (IS at RT = 0.39 mm s^{-1}, area ~80%) and Fe^{2+} (IS at RT = 1.21 mm s^{-1}, area = ~20%). Because Mössbauer areas reflect the fraction of Fe atoms in each state and the Fe stoichiometry of the underlying phases is unknown, we do not convert these values to phase fractions. It is worth mentioning that there is a very close correlation between the Fe Mössbauer spectra valence state areas and the oxidation species calculated from the areas of XPS spectra especially for FeNiBP and FeNiP electrocatalysts, as shown in Table 3. The lack of a fitted Fe^{2+} component in the FeNiP XPS spectrum (Fig. 5c), is because of the higher sensitivity of Mössbauer spectroscopy relative to XPS. For FeNiB, there is a noticeable divergence between the Fe valence states measured by XPS and Mössbauer spectroscopy. This discrepancy most probably indicates a higher percentage of oxidative states at the surface measured by XPS and a higher presence of the near-metallic Fe states at the core of FeNiB. The presence of near-metallic Fe and Ni states only in the FeNiB electrocatalyst, indicates the strong reducing action of $NaBH_4$ in comparison toNaH_2PO_2.

Electrolytic water splitting performance

The self-supported electrocatalysts were evaluated for their HER performance in comparison to that of commercial Pt/C, as shown in Fig. 6. All electrocatalysts demonstrated superior current densities at lower potentials than Pt/C, which exhibited a maximum current density of −358 mA cm^{-2} (Fig. 6a), a Tafel slope of 115 mV dec^{-1} (Fig. 6b), and overpotentials of −0.56 V at −100 mA cm^{-2} and −0.85 V at −300 mA cm^{-2} (Fig. 6c). Among the self-supported electrocatalysts, FeNiB@NF showed the best performance, achieving a maximum current density of −469 mA cm^{-2}. Despite the considerably higher Tafel slope of 257.6 mV dec^{-1}, indicating slower reaction kinetics compared to the other electrocatalysts and a higher charge transfer resistance, indicating slower reaction rate, FeNiB@NF achieved the lowest overpotentials of −0.26 V *vs.* RHE at −100 mA cm^{-2} and −0.52 V *vs.* RHE at −300 mA cm^{-2}, demonstrating higher catalytic activity. FeNiP@NF followed with a maximum current density of −417 mA cm^{-2}, a Tafel slope of 144.2 mV dec^{-1}, and overpotentials of −0.42 V *vs.* RHE at −100 mA cm^{-2} and −0.58 V *vs.* RHE at −300 mA cm^{-2}. The third best-performing electrocatalyst, FeNiBP@NF, showed a maximum current density of −422 mA cm^{-2}, and the lowest Tafel slope among the electrocatalysts at 114.2 mV dec^{-1} comparing to the FeNiB@NF, and overpotentials of −0.44 V *vs.* RHE at −100 mA cm^{-2} and −0.64 V *vs.* RHE at −300 mA cm^{-2}. The superior catalytic activity of FeNiB@NF may be attributed to its much higher ECSA when compared to other electrocatalysts, and to the presence of metallic Fe and Ni species providing higher conductivity, and most likely to a more favourable surface chemistry for water molecules to combine with the surface electrons to form adsorbed hydrogen species (H*). To evaluate the durability of FeNiB@NF at a high current density, chronoamperometry was conducted at −0.63 V *vs.* RHE (~400 mA cm^{-2}) (Fig. 6d). The current density increased by approximately 11% during the first hour and remained stable throughout the 24 hour measurement. This increase is most probably due to the presence of active surface species formed during the electrode's surface reconstruction, as frequently mentioned in the literature for amorphous metal borides.[42] XPS analysis after chronoamperometry, revealed total oxidation of the pure metallic species of Fe and Ni, in conjunction with the formation of Ni^{3+} species (Fig. S5a and b). These chemical changes are most possibly due to the strong oxidative nature of the alkaline electrolyte and the chemical surface reconstruction of the electrocatalysts during the first hour of chronoamperometry. According to SEM images of post HER chronoamperometry (Fig. S5c) there is sufficient electrocatalyst loading on the NF with no noticeable morphological difference in the FeNiB embedded electrocatalyst. These results explain the good durability of the FeNiB@NF electrocatalyst during chronoamperometry, where the current remained stable after the 1 h mark and for the remaining 24 h, as there are no changes in the electrocatalyst loading or morphology. HER can be described by the following mechanism:[2]

$$H_2O + e^- + * \rightarrow H* + OH^-, \quad \text{Volmer reaction} \qquad (5)$$

$$H* + H_2O + e^- \rightarrow H_2 + OH^-, \quad \text{Heyrovsky reaction} \qquad (6)$$

$$H* + H* \rightarrow H_2, \quad \text{Tafel reaction} \qquad (7)$$

To study the bifunctionality of these self-supported electrocatalysts, their behaviour in the OER was evaluated and compared to that of commercial RuO_2, as shown in Fig. 7. All of the self-supported electrocatalysts exhibited industrial-scale current densities and achieved lower overpotentials at 100 mA cm^{-2} compared to RuO_2, indicating a higher catalytic activity with less energy required to drive the OER.[43] Overall, all three electrocatalysts exhibited comparable OER performance providing useful insight for their rational design, suggesting that they most likely operate through similar

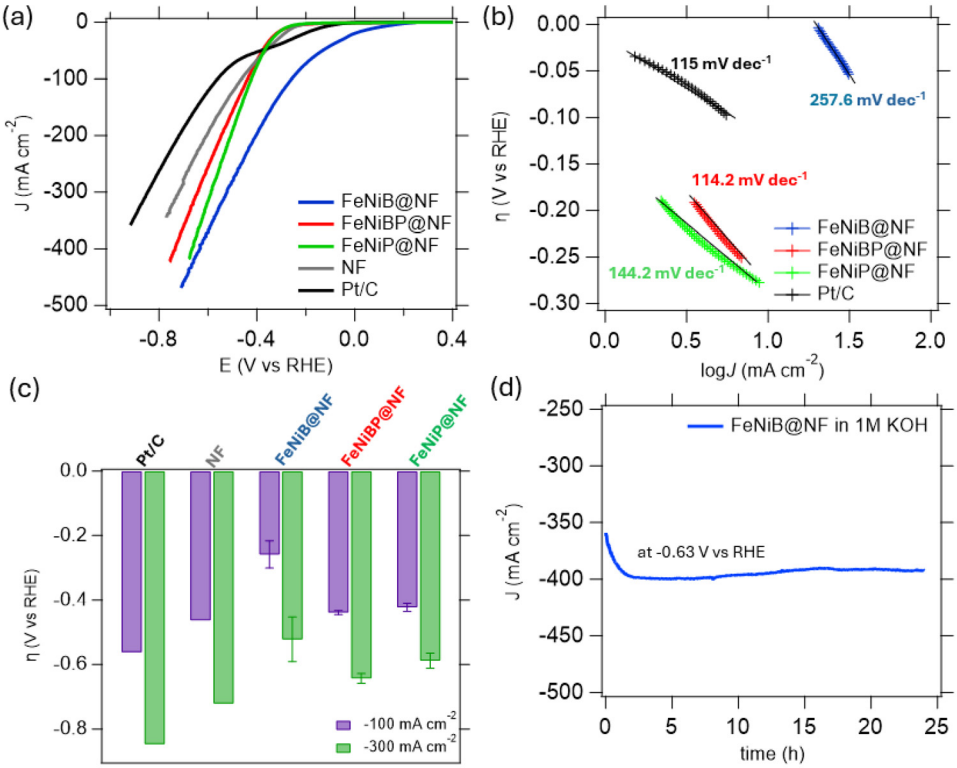

Fig. 6 Polarisation curves (a), Tafel slopes (b), overpotentials at −100 mA cm^{-2} and −300 mA cm^{-2} (c) for HER activity, chronoamperometric curve (d) of FeNiB@NF at −0.63 V (*vs.* RHE) for 24 h in 1 M KOH.

surface-transformed active species and/or closely related reaction pathways under OER conditions. Therefore, the absence of a significant performance difference is itself an important finding, with practical relevance for future catalyst design and technological development. In addition, it is worth noting that polarisation curve of FeNiB@NF did not start at zero current density as the other two electrocatalysts. This phenomenon can be attributed to the fact that at the beginning of the potential sweep, a non-faradaic current arises from charging of the electrochemical double layer at the electrode–electrolyte interface. This capacitive current exists even before any Faradaic OER reaction occurs and results in a non-zero baseline current. In Table S4 the determined double layer capacitance is presented for three electrocatalysts with the FeNiB@NF exhibiting a capacitance 30 times higher compared to the other two electrocatalysts. In more detail, the FeNiBP@NF demonstrated the highest performance, achieving a maximum current density of 972 mA cm^{-2} (Fig. 7a) and low overpotentials of 0.37 V *vs.* RHE at 100 mA cm^{-2} and 0.54 V *vs.* RHE at 300 mA cm^{-2} (Fig. 7c), and a Tafel slope (Fig. 7b) of 51.6 mV dec^{-1}, indicating faster reaction kinetics compared to RuO_2. FeNiB@NF, which was the best-performing HER electrocatalyst, exhibited a current density of 954 mA cm^{-2}, a Tafel slope of 274.7 mV dec^{-1}, and overpotentials of 0.36 V *vs.* RHE at 100 mA cm^{-2} and 0.55 V *vs.* RHE at 300 mA cm^{-2}. The lowest performing electrocatalyst was FeNiP@NF, which achieved a current density of 930 mA cm^{-2}, Tafel slope similar to FeNiBP@NF at 51.6 mV dec^{-1}, and overpotentials of 0.40 V *vs.* RHE at 100 mA cm^{-2} and 0.58 V *vs.* RHE at 300 mA cm^{-2}. This superior activity of FeNiBP@NF is believed to stem from its surface chemistry and the synergistic effects of boron and phosphorus, which likely facilitate OH* adsorption during the initial stages of OER and subsequent formation of O* and *OOH species, as shown in the suggested mechanisms in the following section. Most probably, the lower charge transfer resistance of FeNiBP@NF and homogeneous catalyst distribution on the NF are crucial for the better OER activity.

FeNiBP@NF was chosen for chronoamperometry testing conducted at 2.14 V *vs.* RHE (~760 mA cm^{-2}) (Fig. 7d). A sharp increase of approximately 10% was observed between the first and second hour of the 24 hour measurement, which may be attributed to a favourable surface reconstruction and formation of the active NiOOH and FeOOH species, followed by a steady decline of 10% from the initial current density.[44] According to post-OER chronoamperometry XPS analysis on the FeNiBP@NF electrocatalyst (Fig. S6a and b), a significant increase of Fe^{2+} and a decline in of Fe^{3+} species was observed. The same trend was observed at the Ni^{2+} and Ni^{3+} species (Table S6). SEM images of post-OER chronoamperometry (Fig. S6c) indicated that a sufficient amount of electrocatalyst particles on NF still remains, with a noticeable sintering effect having occurred. This sintering effect, which resulted in a lower surface area of the electrocatalyst on the NF, may be

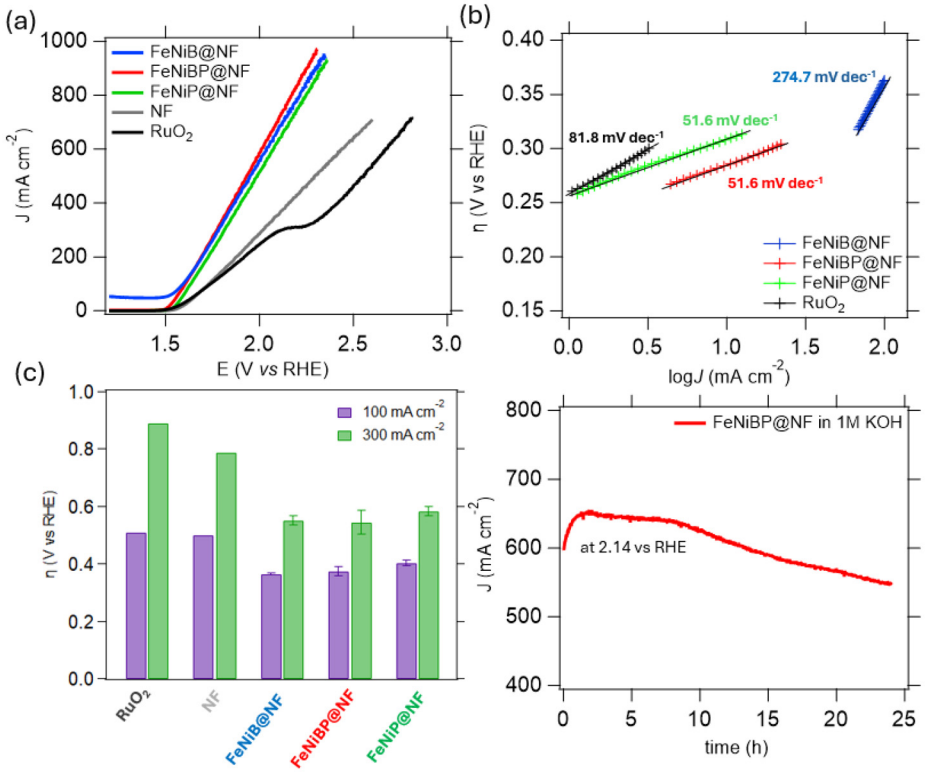

Fig. 7 Polarisation curves (a), Tafel slopes (b), overpotentials at 100 mA cm^{-2} and 300 mA cm^{-2} (c) for OER activity, chronoamperometric curve (d) of FeNiBP@NF at 2.14 V (*vs.* RHE) for 24 h in 1 M KOH.

responsible for the downward trend in the current density during the chronoamperometry testing.

The suggested OER mechanism is described below.[45]

$$OH^- + * \rightarrow OH* + e^- \quad (8)$$

$$OH* + OH^- \rightarrow O* + H_2O + e^- \quad (9)$$

$$O* + OH^- \rightarrow *OOH + e^- \quad (10)$$

$$*OOH + OH^- \rightarrow * + O_2 + H_2O + e^- \quad (11)$$

$$O* + O* \rightarrow O_2 \quad (12)$$

To investigate the relationship between surface properties and the activity of the electrocatalysts, electrochemical surface area (ECSA) was measured 1 M KOH electrolyte. Fig. S4 shows the CV curves at scan rates of 20, 40, 60, 80, 100, and 120 mV s^{-1}. Interestingly, both C_{dl} and ECSA values were orders of magnitude higher for the FeNiB@NF electrocatalyst. This may be attributed to the presence of metallic Fe and Ni present in this electrocatalyst. However, the higher ECSA and C_{dl} where not accompanied by increased catalytic activity in OER. Table S4 presents the C_{dl} values for FeNiB@NF, FeNiBP@NF, and FeNiP@NF as 15.08, 0.52, and 0.51 mF cm^{-2}, respectively. The corresponding ECSA values for FeNiB@NF, FeNiBP@NF, and FeNiP@NF were 377.2, 13.1, and 12.9 cm^2, respectively. The kinetics of the HER and OER were further studied using EIS (Fig. S1), specifically by comparing the charge transfer resistance values normalised by the geometrical surface area for each electrocatalysts (Table S2). FeNiB@NF, exhibited the highest normalised charge transfer resistance of 92.43 Ω cm^2, surpassing FeNiBP@NF (79.33 Ω cm^2) and FeNiP@NF (70.61 Ω cm^2). This may indicate that charge transfer resistance, and thus electronic conductivity, is a more important factor for catalytic activity than the electrochemical active surface area.

Ammonia-rich alkaline simulated wastewater electrolysis performance

The best-performing HER electrocatalyst, FeNiB@NF, was further examined in 1 M KOH + 0.33 M NH_3 electrolyte to assess its hydrogen evolution behaviour under ammonia-rich alkaline conditions. FeNiB@NF achieved a maximum current density of −330 mA cm^{-2} notably lower than the −469 mA cm^{-2} maximum current density in the alkaline water electrolyte (Fig. 8a). The Tafel slope in the ammonia-rich electrolyte was correspondingly 428.3 mV dec^{-1} (Fig. 8b), indicating significantly hindered reaction kinetics and a greater energetic demand. Similarly, FeNiB@NF required notably more negative potentials to drive HER in the presence of NH_3, achieving overpotentials of −0.34 V at −100 mA cm^{-2} and −0.66 V at −300 mA cm^{-2} (Fig. 8c). Chronoamperometry at −0.66 V *vs.* RHE (~300 mA cm^{-2}) (Fig. 8d) further revealed the impact of NH_3 on long-term stability. The current initially increased by ~12%, likely due to early interfacial rearrangement, but subsequently exhibited a steady decline, likely suggesting pro-

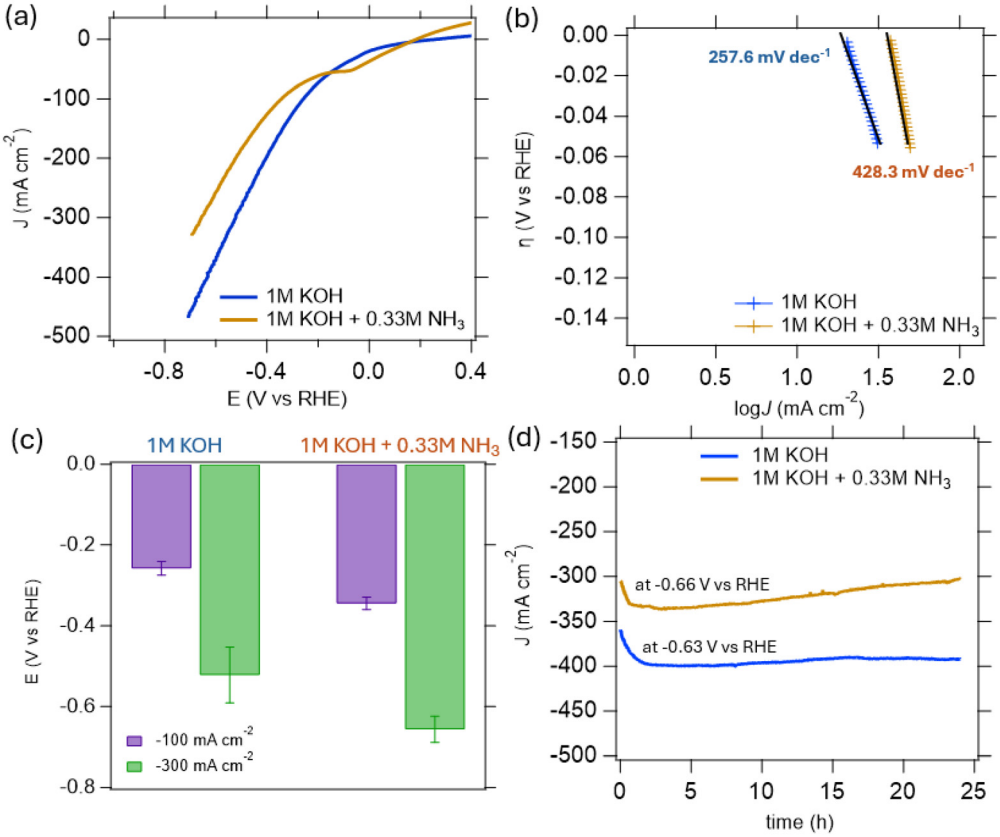

Fig. 8 Comparison of polarisation curves (a), Tafel slopes (b), potentials at −100 mA cm^{-2} and −300 mA cm^{-2} (c) and chronoamperometric curves (d) for 24 h of FeNiB@NF at −0.66 V (*vs.* RHE) in 1 M KOH + 0.33 M NH_3 and at −0.63 V (*vs.* RHE) 1 M KOH.

gressive surface inhibition by NH_x species. Impedance results (Fig. S7 and Table S5) also confirmed modified interfacial behaviour in the ammonia-containing electrolyte, consistent with altered double-layer characteristics and charge-transfer dynamics.

Similarly to post-HER in alkaline water chronoamperometry, XPS analysis of the FeNiB@NF electrocatalyst after HER chronoamperometry in ammonia-rich electrolyte revealed total oxidation of metallic Fe, a substantial increase in the Fe^{3+} fraction accompanied by a corresponding decrease in Fe^{2+} (Fig. S8a and Table S6). For nickel (Fig. S8b), the metallic Ni was totally oxidised and the proportion of Ni^{2+} decreased from 61.7% to 51.8%, while Ni^{3+} constituted a 48.2% spectra area (Table S6). Post-HER chronoamperometry SEM images in ammonia-rich electrolyte (Fig. S8c) indicated the absence of sintering effects and almost no catalyst particles removal form the NF. Overall, these findings establish that while FeNiB@NF remains active in ammonia-rich alkaline electrolyte, NH_3 imposes significant kinetic and stability limitations, leading to higher overpotentials, slower electron-transfer rates, and reduced long-term performance compared to pure KOH.

To evaluate the AOR electrocatalytic activity in ammonia-rich alkaline water, the best-performing self-supported electrocatalyst in OER, FeNiBP@NF, was chosen. This selection was made due to the mechanistic overlap in oxidative pathways under alkaline conditions, which may suggested that the FeNiBP@NF self-supported electrocatalyst could also exhibit promising activity toward AOR.[46] Its performance was thoroughly examined in an ammonia-rich alkaline electrolyte of 1 M KOH + 0.33 M NH_3, as presented in Fig. 9. FeNiBP@NF exhibited higher current densities at lower applied potentials in the AOR compared to the OER, validating FeNiBP@NF as an effective electrocatalyst for the ammonia oxidation reaction. For AOR, the electrocatalyst achieved a high current density equal to 963 mA cm^{-2} at 1.97 V *vs.* RHE (Fig. 9a) and demonstrated potentials of 1.57 V *vs.* RHE at 100 mA cm^{-2} and 1.67 V *vs.* RHE at 300 mA cm^{-2} (Fig. 9c). Comparatively, FeNiBP@NF in OER achieved a current density of 972 mA cm^{-2} at 2.3 V *vs.* RHE and potentials of 1.60 V at 100 mA cm^{-2} and 1.77 V at 300 mA cm^{-2}. FeNiBP@NF exhibited a higher Tafel slope in AOR than in OER, reaching 82 mV dec^{-1} for AOR compared to 51.6 mV dec^{-1} for OER (Fig. 9b), indicating less favourable reaction kinetics in the ammonia-rich electrolyte. However, the lower charge-transfer resistance measured in the ammonia-rich electrolyte (Fig. S7 and Table S5) may suggest that this trend is unlikely to arise from hindered interfacial charge transfer and may instead reflect the multielectron AOR reaction pathway. To evaluate FeNiBP@NF's long-term stability in AOR at a high current density (~760 mA cm^{-2}), chronoamperometry was performed for 24 h at 1.88 V *vs.* RHE (Fig. 9d). The

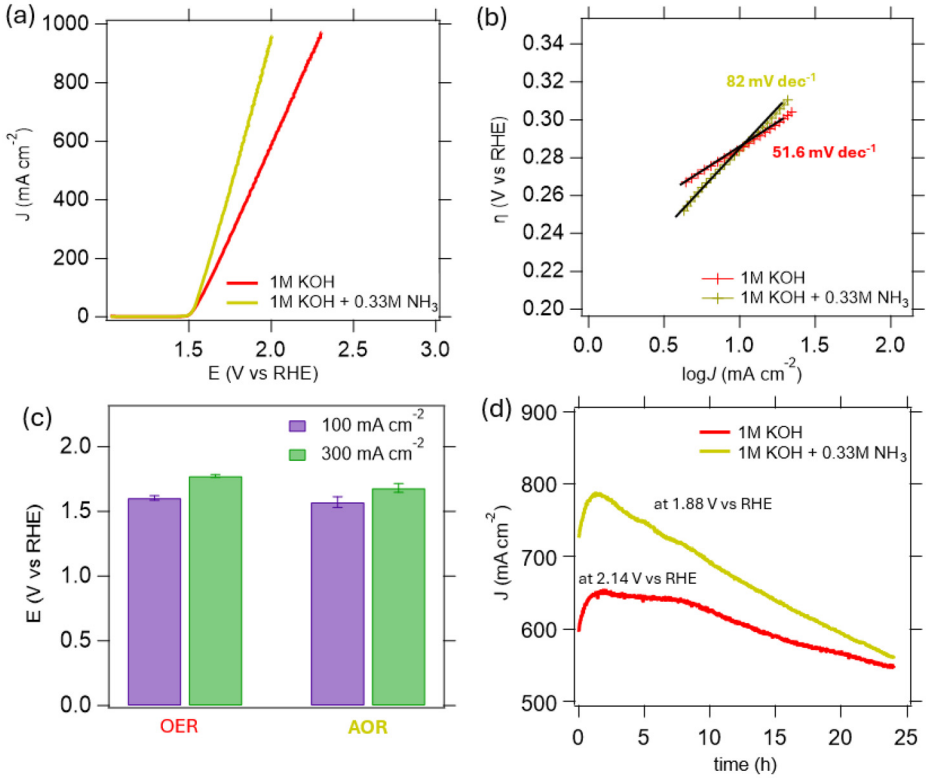

Fig. 9 Comparison of polarisation curves (a), Tafel slopes (b), potentials at 100 mA cm^{-2} and 300 mA cm^{-2} (c) and chronoamperometric curves (d) for 24 h of FeNiBP@NF at 1.88 V (*vs.* RHE) in 1 M KOH + 0.33 M NH_3 and at 2.14 V (*vs.* RHE) in 1 M KOH.

initial activation phase during AOR led to a notable increase in current of 8%, but the catalyst showed a sharper decline afterward, likely due to the harsher ammonia containing environment, N_2 catalysts poisoning and partial NH_3 depletion; suggesting that the electrocatalyst's stability under long-term operation in AOR may require further optimisation.

Post-AOR chronoamperometry XPS analysis on the FeNiBP@NF electrocatalyst revealed a moderate increase of Fe^{2+} with a significant decline in Fe^{3+} (Table S6). However, a peak at 704.1 eV appeared, indicating the presence of metallic Fe (Fig. S9a). This apparent metallic reduction pattern may be attributed to the action of reducing intermediates generated during AOR, such as hydrazine species, which are capable of partially reducing the high-valent Ni/Fe oxyhydroxide surface back to lower oxidation states. Regarding Ni (Fig. S9b), Ni^{2+} area before AOR was 28.6% and after 33.6%, while for Ni^{3+} species before AOR was 71.4% and after 66.4% (Table S6). To better understand these underlying phenomena *in situ* XPS analysis could provide valuable information. SEM imaging after AOR chronoamperometry (Fig. S9c) revealed a sufficient amount of FeNiBP nanoparticles on NF, suggesting minimal catalyst removal, however noticeable sintering particles are observed, which most probably contributed to the decline in the current density pattern.

For the purpose of defining the evolution of the intermediate surface species on FeNiBP@NF during LSV in 1 M KOH and 1 M KOH + 0.33 M NH_3 *operando* DRIFTS (Fig. 10) was employed. In alkaline electrolyte (Fig. 10a), the progressive growth of the broad O–H stretching envelope between 3250–3750 cm^{-1}, together with the development of bands in the 800–1700 cm^{-1} region, is consistent with the formation of M–OH/M–OOH species in line with the commonly observed reconstruction of Fe–Ni catalysts into oxyhydroxide phases during OER.[47,48]

In the ammonia-rich electrolyte (Fig. 10b), additional features appear at substantially lower potentials. Bands at around 950–970 cm^{-1}, 1220 cm^{-1}, 1370–1420 cm^{-1}, 1600–1650 cm^{-1} and near 3300–3350 cm^{-1} can be attributed to various NH_3-derived and N–O containing intermediates such as volatile or weakly absorbed NH_3, molecularly adsorbed NH_3, NH_4^+/amide species, nitrite species, and N–H stretching vibrations, respectively.[49–51] This indicates that ammonia related species occupy a significant fraction of the surface. The comparatively strong intensity of these N-containing vibrations suggests that the catalyst surface shows a pronounced preference for ammonia-derived intermediates over purely OER-related oxyhydroxide species in this potential window, consistent with the lower thermodynamic requirement of AOR and the high affinity of the surface for NH_3. Accordingly, the AOR is widely recognised to proceed *via* the Gerischer–Mauerer mechanism in alkaline media, which is detailed as follows:[11,52]

$$NH_3 + OH^- + * \rightleftharpoons NH_2* + H_2O + e^- \quad (13)$$

$$NH_2* + OH^- \rightarrow NH* + H_2O + e^- \quad (14)$$

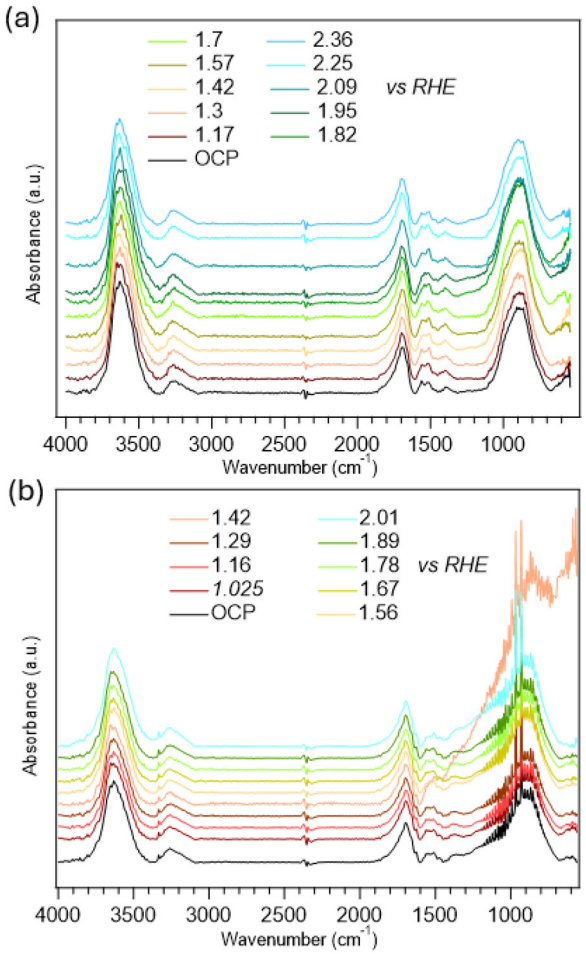

Fig. 10 *Operando* DRIFTS spectra of FeNiBP@NF recorded during LSV in 1.0 M KOH (a) and 1.0 M KOH + 0.33 M NH_3 (b).

$$NH* + OH^- \rightarrow N* + H_2O + e^- \quad (15)$$

$$NH_x* + NH_y* \rightarrow H_xNNH_y* + * \quad (16)$$

$$H_xNNH_y* + (x+y)OH^- \rightarrow N_2* + (x+y)H_2O + (x+y)e^- + * \quad (17)$$

To further examine the practical performance of the FeNiB@NF and FeNiBP@NF electrodes, a two-electrode FeNiBP@NF||FeNiB@NF cell was assembled and tested in both 1 M KOH and 1 M KOH + 0.33 M NH_3 (Fig. S10). In 1 M KOH (Fig. 11), the cell delivered 10 mA cm^{-2} at 1.71 V, reaching a maximum current density of 45.6 mA cm^{-2} at 2.0 V, while the introduction of ammonia reduced the required cell voltage, achieving 10 mA cm^{-2} at 1.65 V with a maximum of 47.0 mA cm^{-2} at 2.0 V. These values provide a reasonable benchmark comparison, acknowledging that the present configuration is a simple non-zero-gap cell with a relatively large electrode spacing. Therefore, the obtained current densities likely underestimate the intrinsic activity of the catalyst pair. In a true zero-gap configuration, where the anode and cathode are separated only by a membrane/diaphragm, the ionic resistance is minimised, and therefore higher current densities would be expected. Thus, the present results should be interpreted as a fundamental evaluation of catalyst-pair performance, while further optimisation of cell architectures and reactor designs will be necessary for industrially relevant operation.

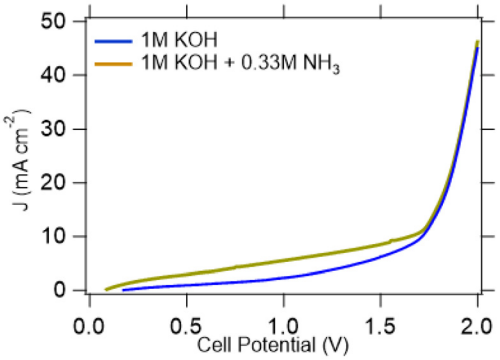

Fig. 11 Cell potential polarisation curves of FeNiBP@NF||FeNiB@NF water electrolysis in 1 M KOH and in ammonia-rich simulated wastewater electrolyte in 1 M KOH + 0.33 M NH_3.

Conclusions

In this work, a green, scalable chemical reduction strategy was employed to synthesise self-supported FeNiB, FeNiBP, and FeNiP electrocatalysts on nickel foams. Structural and surface analysis confirmed that tuning the B/P ratio, modulates their physiochemical properties and electrocatalytic behaviour as expected. Sodium borohydride acted as a very strong reducing agent, resulting in FeNiB@NF with metallic Fe and Ni states and a high electrochemical active surface area, exhibiting the most efficient HER activity in alkaline and in ammonia-rich wastewater-simulated alkaline environments. Whereas, FeNiBP@NF, with its synergistic B/P electronic modulation and homogeneous distribution on NF, demonstrated remarkable OER and AOR activity, achieving industrial-scale current densities. Stability assessments revealed robust HER stability and a very satisfying OER durability, while long-term AOR and HER stability in ammonia-rich electrolytes require further optimisation due to catalyst poisoning and partial reduction by reactive intermediates. These findings provide critical insights into the interplay between surface chemistry and morphology in dictating trifunctional electrocatalytic performance. Beyond alkaline water electrolysis, the ability to operate in ammonia-rich alkaline electrolytes underscores the dual environmental and energy benefits of this approach through the potential utilisation of ammonia-rich alkaline wastewater streams. The design principles outlined here offer a rational pathway for the broader development of earth-abundant, self-supported electrocatalysts *via* a simple synthesis method capable of meeting the demands for scalable green hydrogen production and water recycling.

Author contributions

All authors contributed at the writing of this manuscript and given approval to the final version.

Conflicts of interest

There are no conflicts to declare.

Data availability

The majority of the data supporting this article have been included as part of the supplementary information (SI). Supplementary information: additional materials characterisations and electrochemical measurements. See DOI: https://doi.org/10.1039/d5nr05371d.

Additional data that support the findings of this work are available from the corresponding author upon reasonable request.

Acknowledgements

T. K. and M. V. S. acknowledges the financial support from the Government of Ireland Postgraduate Scholarship with project ID GOIPG/2024/4638, the UCD Ad Astra fellowship programme, the UCD College of Engineering and Architecture Career Development Award and the Royal Chemical Society for the Research Enablement Grant #72049. HR-TEM and EDX analysis were performed at the SFI-funded CRANN Advanced Microscopy Laboratory (AML). The UCD School of Chemistry is gratefully acknowledged for financial support. L. N. wishes to thank Science Foundation Ireland for their support (grant number 22/FFP-P/11527). Special thanks to Prof. James Sullivan for providing access to his laboratory facilities. Dr Tan is acknowledged for the great help with *operando* measurements.

References

1 J. A. Turner, *Science*, 1999, **285**, 687–689.
2 J. Wang, X. Yue, Y. Yang, S. Sirisomboonchai, P. Wang, X. Ma, A. Abudula and G. Guan, *J. Alloys Compd.*, 2020, **819**, 153346.
3 Z. Wu, X. F. Lu, S. Zang and X. W. (David) Lou, *Adv. Funct. Mater.*, 2020, **30**, 1910274.
4 G. S. Cassol, C. Shang, A. K. An, N. K. Khanzada, F. Ciucci, A. Manzotti, P. Westerhoff, Y. Song and L. Ling, *Nat. Commun.*, 2024, **15**, 2617.
5 A. A. Shah, S. Walia and H. Kazemian, *J. Environ. Chem. Eng.*, 2024, **12**, 114420.
6 A. AlZaabi, F. AlMarzooqi and D. Choi, *Int. J. Hydrogen Energy*, 2024, **94**, 23–52.
7 L. A. Diaz and G. G. Botte, *Ind. Eng. Chem. Res.*, 2012, **51**(38), 12167–12172.
8 J. Wang, S. Qing, X. Tong, K. Zhang, G. Luo, J. Ding and L. Xu, *Appl. Surf. Sci.*, 2023, **640**, 158330.
9 Y. Ji, A. Ozden, S. Chen, C. Yang and M. Luo, *J. Mater. Chem. A*, 2025, **13**, 20176–20199.
10 S. Hu, Y. Tan, C. Feng, H. Wu, J. Zhang and H. Mei, *J. Power Sources*, 2020, **453**, 227872.
11 P. Babar and G. G. Botte, *ACS Sustainable Chem. Eng.*, 2024, **12**, 13030–13047.
12 E. Latvytė, X. Zhu, L. Wu, R. Lan, P. Vale and J. E. Graves, *Int. J. Hydrogen Energy*, 2024, **52**, 265–282.
13 H.-Y. Sun, G.-R. Xu, F.-M. Li, Q.-L. Hong, P.-J. Jin, P. Chen and Y. Chen, *J. Energy Chem.*, 2020, **47**, 234–240.
14 H. Kim, S. Hong, H. Kim, Y. Jun, S. Y. Kim and S. H. Ahn, *Appl. Mater. Today*, 2022, **29**, 101640.
15 A. Salehabadi, J. Zanganeh and B. Moghtaderi, *Int. J. Hydrogen Energy*, 2024, **63**, 828–843.
16 T. E. Bell and L. Torrente-Murciano, *Top. Catal.*, 2016, **59**, 1438–1457.
17 S. He, Y. Chen, M. Wang, H. Nuomin, P. Novello, X. Li, S. Zhu and J. Liu, *Nano Energy*, 2021, **80**, 105528.
18 S. Carenco, D. Portehault, C. Boissière, N. Mézailles and C. Sanchez, *Chem. Rev.*, 2013, **113**, 7981–8065.
19 X. Li, Z. Zhang, M. Shen, Z. Wang, R. Zheng, H. Sun, Y. Liu, D. Wang and C. Liu, *J. Colloid Interface Sci.*, 2022, **628**, 242–251.
20 F.-G. Wang, L. Xin, Q.-X. Lv, B. Liu, Y.-M. Chai and B. Dong, *Chin. J. Struct. Chem.*, 2022, **41**, 2209008–2209044.
21 E. J. Popczun, J. R. McKone, C. G. Read, A. J. Biacchi, A. M. Wiltrout, N. S. Lewis and R. E. Schaak, *J. Am. Chem. Soc.*, 2013, **135**, 9267–9270.
22 Y. Zhan, T. Yang, S. Liu, L. Yang, E. Wang, X. Yu, H. Wang, K.-C. Chou and X. Hou, *Nanomaterials*, 2025, **15**, 917.
23 A. Ashok Kashale, C.-T. Wu, H.-F. Hsu and I.-W. Peter Chen, *Chem. Eng. J.*, 2023, **474**, 145907.
24 P. T. Pham, S. H. Roh, J. Y. Kim and J. K. Kim, *J. Ind. Eng. Chem.*, 2025, **152**, 136–154.
25 K. Jiang, K. Li, Y.-Q. Liu, S. Lin, Z. Wang, D. Wang and Y. Ye, *Electrochim. Acta*, 2022, **403**, 139700.
26 C. Jo, S. Surendran, M.-C. Kim, T.-Y. An, Y. Lim, H. Choi, G. Janani, S. C. Jesudass, D. J. Moon, J. Kim, J. Y. Kim, C. H. Choi, M. Kim, J. K Kim and U. Sim, *Chem. Eng. J.*, 2023, **463**, 142314.
27 W. Zheng, M. Liu and L. Y. S. Lee, *ACS Energy Lett.*, 2020, **5**, 3260–3264.
28 B. Schmitt, E. Murphy, S. J. Trivedi, Q. Zhang, B. J. Rodriguez, A. Rafferty, R. Bekarevich, G. Ersek, G. Portale and M. V. Sofianos, *Sustainable Energy Fuels*, 2024, **8**, 5793–5805.
29 P. T. Anastas and J. C. Warner, *Green Chemistry: Theory and Practice*, Oxford University Press, New York, 1998.
30 S. Brunauer, P. H. Emmett and E. Teller, *J. Am. Chem. Soc.*, 1938, **60**, 309–319.
31 E. P. Barrett, L. G. Joyner and P. P. Halenda, *J. Am. Chem. Soc.*, 1951, **73**, 373–380.

32 A. P. Douvalis, A. Polymeros and T. Bakas, *J. Phys.: Conf. Ser.*, 2010, **217**, 012014.
33 S. Anantharaj and S. Noda, *J. Mater. Chem. A*, 2022, **10**, 9348–9354.
34 G. Liu, D. He, R. Yao, Y. Zhao and J. Li, *Nano Res.*, 2018, **11**, 1664–1675.
35 Y. Zhao, F. Ma, Z. Wang, P. Wang, Y. Liu, H. Cheng, Y. Dai, Z. Zheng and B. Huang, *J. Alloys Compd.*, 2022, **903**, 163741.
36 J. Kwon, H. Han, S. Jo, S. Choi, K. Y. Chung, G. Ali, K. Park, U. Paik and T. Song, *Adv. Energy Mater.*, 2021, **11**, 2100624.
37 P. Yang, Y. Liu, R. Su, P. He and S. Huang, *Int. J. Hydrogen Energy*, 2024, **49**, 1490–1498.
38 M. Qin, J. Ye, G. Ma, Z. Fan, L. Huang and X. Xin, *Small*, 2025, **21**, 2502054.
39 Y. Sheng, M. Manuputty, M. Kraft and R. Xu, *ACS Appl. Energy Mater.*, 2023, **6**, 2320–2332.
40 Y. Yao, S. Wang, X. Song, Y. Liu, J. Wang and S. Wang, *Chem. Eng. Sci.*, 2025, **314**, 121801.
41 J. Yu, H. Jing, P. Zhao, K. Lu, J. Song, Z. Wu, H. Wu, B. Liu, W. Lei and Q. Hao, *J. Mater. Chem. A*, 2022, **10**, 2035–2044.
42 C. Chen, C. Du, Z. Wang, X. Chen, Y. Wang, N. Ju, Y. Fu, Z. Liu, M. Jia, S. Luo, G. Xu, J. Xu and H. Sun, *Energy Fuels*, 2025, **39**, 12154–12164.
43 H. Sun, X. Xu, H. Kim, W. Jung, W. Zhou and Z. Shao, *Energy Environ. Mater.*, 2023, **6**, e12441.
44 M. Tang, Y.-M. He, A. Ali, J.-L. Zhu, P.-K. Shen and Y.-F. Ouyang, *Int. J. Hydrogen Energy*, 2022, **47**, 28303–28312.
45 X. Xie, L. Du, L. Yan, S. Park, Y. Qiu, J. Sokolowski, W. Wang and Y. Shao, *Adv. Funct. Mater.*, 2022, **32**, 2110036.
46 H. Liu, X. Xu, D. Guan and Z. Shao, *Energy Fuels*, 2024, **38**, 919–931.
47 E. M. Kazek, R. Villano, M. V. Sofianos, J. Z. Y. Tan and L. Negahdar, *Catal. Sci. Technol.*, 2025, **15**, 4392–4405.
48 E. Healy, Q. Zhang, B. J. Rodriguez, A. Rafferty, R. Bekarevich, G. Ersek, G. Portale, R. Villano, L. Negahdar and M. V. Sofianos, *Mater. Today Energy*, 2025, **52**, 101958.
49 H. Hu, S. Cai, H. Li, L. Huang, L. Shi and D. Zhang, *J. Phys. Chem. C*, 2015, **119**, 22924–22933.
50 C. Mao, J. Wang, Y. Zou, Y. Shi, C. J. Viasus, J. Y. Y. Loh, M. Xia, S. Ji, M. Li, H. Shang, M. Ghoussoub, Y.-F. Xu, J. Ye, Z. Li, N. P. Kherani, L. Zheng, Y. Liu, L. Zhang and G. A. Ozin, *J. Am. Chem. Soc.*, 2023, **145**, 13134–13146.
51 C. Yu, L. Wang and B. Huang, *Aerosol Air Qual. Res.*, 2015, **15**, 1017–1027.
52 J. A. Herron, P. Ferrin and M. Mavrikakis, *J. Phys. Chem. C*, 2015, **119**, 14692–14701.